Investigating Effects of Heterogeneity and Fracture Distribution on Two-Phase Flow in Fractured Reservoir with adaptive time strategy

Wang, Lu Yu; Chen, Wei Zhong; Zhang, Yan Jun; Zhang, Xiao Dong; Vuik, Cornelis

DOI
10.1007/s11242-022-01850-z

Publication date
2023

Document Version
Final published version

Published in
Transport in Porous Media

Citation (APA)
Wang, L. Y., Chen, W. Z., Zhang, Y. J., Zhang, X. D., & Vuik, C. (2023). Investigating Effects of Heterogeneity and Fracture Distribution on Two-Phase Flow in Fractured Reservoir with adaptive time strategy. *Transport in Porous Media*, *149*(1), 175-203. https://doi.org/10.1007/s11242-022-01850-z

Transport in Porous Media
https://doi.org/10.1007/s11242-022-01850-z

S.I.: GEOLOGICAL SYSTEMS WITH FRACTURED POROUS MEDIA

Investigating Effects of Heterogeneity and Fracture Distribution on Two-Phase Flow in Fractured Reservoir with adaptive time strategy

Lu-Yu Wang[1,5] · **Wei-Zhong Chen**[2] · **Yan-Jun Zhang**[4] · **Xiao-Dong Zhang**[5] · **Cornelis Vuik**[3]

Received: 4 July 2022 / Accepted: 22 August 2022

Abstract

Modeling of fluid flow in porous media is a pillar in geoscience applications. Previous studies have revealed that heterogeneity and fracture distribution have considerable influence on fluid flow. In this work, a numerical investigation of two-phase flow in heterogeneous fractured reservoir is presented. First, the discrete fracture model is implemented based on a hybrid-dimensional modeling approach, and an equivalent continuum approach is integrated in the model to reduce computational cost. A multilevel adaptive strategy is devised to improve the numerical robustness and efficiency. It allows up to 4-levels adaption, where the adaptive factors can be modified flexibly. Then, numerical tests are conducted to verify the the proposed method and to evaluate its performance. Different adaptive strategies with 3-levels, 4-levels and fixed time schemes are analyzed to evaluate the computational cost and convergence history. These evaluations demonstrate the merits of this method compared to the classical method. Later, the heterogeneity in permeability field, as well as initial saturation, is modeled in a layer model, where the effect of layer angle and permeability on fluid flow is investigated. A porous medium containing multiple length fractures with different distributions is simulated. The fine-scale fractures are upscaled based on the equivalent approach, while the large-scale fractures are retained. The conductivity of the rock matrix is enhanced by the upscaled fine-scale fractures. The difference of hydraulic property between homogeneous and heterogeneous situations is analyzed. It reveals that the heterogeneity may influence fluid flow and production, while these impacts are also related to fracture distribution and permeability.

Article highlights

- A multilevel adaptive implicit scheme up to 4-levels adaption is presented for two-phase ow in heterogeneous fractured reservoir.
- Discrete fracture model is combined with an equivalent continuum approach to reduce the complexity of fracture networks.

✉ Lu-Yu Wang
luyu.wang@hotmail.com

Extended author information available on the last page of the article

- The effects of permeability, orientation, size and number of fractures on hydraulic properties are studied.
- A comparison study of fluid flow and numerical performance between homogeneous and heterogeneous media is conducted.

Keywords Fractured porous media · Two-phase flow · Heterogeneity · Fracture distribution · Multilevel adaptive scheme

1 Introduction

Modeling and simulation of fluid flow and transport in geomaterials is of paramount important in geoscience applications and geotechnical engineering, for instance, reservoir engineering, energy storage, radioactive waste disposal, hydraulic and water resources engineering (Sahimi 2011; Adler et al. 2013; Medici et al. 2021). Investigations on porous media, in which the natural fractures are absent, are well understood and are more mature than that of the fractured porous media (Ghorbani et al. 2016; Badar and Tirumkudulu 2020). Recent decades, much attention has been focused on the development of numerical methods of fluid flow in fractured media. Several numerical challenges are raised, typically mesh partition on a complex fracture network (Mustapha 2014), modeling of multiscale feature of discrete fractures (Molins et al. 2019) and robustness of numerical methods (Pandare and Luo 2018). Especially, the presence of multiple length fractures makes simulators more unstable compared to the case without fractures. Moreover, the inherent features of a geological field, for instance, the heterogeneity, create the challenge on numerical stability and accuracy. To this end, this work focuses on numerical simulation of fractured porous media and study the effect of heterogeneity on hydraulic properties.

The complicated topological geometry of the fracture networks is an essential characteristic of the fractured porous media. Therefore, the challenges induced by modeling stochastic fractures have been paid much attention (Berre et al. 2019; Wang et al. 2019a, 2020; Tan et al. 2021). The discrete fracture network (DFN) was first proposed (Long and Billaux 1987; Cacas et al. 1990) to model single-phase flow only in discrete fractures, where the flow in the rock matrix is neglected in this model. It is a simplified model with an assumption that fractures have high conductivity and the rock bulk is almost impermeable. An enhanced version of DFN, based on the concept of fractured porous media, was proposed for modeling fluid flow in both the rock matrix and discrete fractures, where the flux interaction between them is allowed (Hoteit and Firoozabadi 2008b; Choo and Lee 2018; Berre et al. 2019). Meanwhile, combined with the finite difference, finite element and finite volume methods, the DFN-based methods have gained many successes in simulation of hydraulic process as well as mechanical deformation (Gupta and Duarte 2018; Wang et al. 2019b, 2020; Hosseini and Khoei 2021; Wang et al. 2022).

On the basis of the concept of fractured porous media, there are two representative models classified by the conformal and non-conformal meshes, namely the discrete fracture model (DFM) (Karimi-Fard et al. 2004; Hoteit and Firoozabadi 2008b; Wang et al. 2022) and the embedded discrete fracture model (EDFM) (Hajibeygi et al. 2011; Tene et al. 2017). Both of them have pros and cons. EDFM enjoys mesh independence between the rock matrix and fractures. But the accuracy highly depends on the interpolation points in fractures and the flux transfer function. The DFM has been applied in many geoscience applications, in which one does not need to consider the transfer function between fractures and rock matrix, and the grids are partitioned along each fracture in a conformal scheme. In this work, the DFM is selected as a prototype of the proposed numerical method. The advantages of DFM are accuracy and it follows the strict formulations of finite element and finite volume methods. Therefore, the fractures are modeled as the low-dimensional objects along the interfaces of matrix cells.

The heterogeneity in permeability field would lead to the numerical instability of a simulator and an ill-convergence condition may occur (Chung et al. 2018). In the past decades, many numerical methods have been developed for heterogeneous porous media. The multiscale modeling approach was developed, where the information about the dual and primal grids is required for the multiscale solver (Wang et al. 2014). A discontinuous control volume finite element method was proposed (Salinas et al. 2018), in which the pressure has 1st-order accuracy and that of velocity is 2nd-order. Lately, a novel method, namely the fracture cross-flow equilibrium (Zidane and Firoozabadi 2020), was devised to model flow in non-planar fractures. The lattice Boltzmann method was combined with image segmentation techniques (Liu et al. 2020) to simulate multi-phase flow at different scales. On the other hand, the capillary heterogeneity can also affect the flow path in fractured reservoirs. A numerical challenge behind it is the treatment of saturation discontinuity in finite element framework. In addition, the contrast in capillary pressure function in heterogeneous media may cause the capillary discontinuity then induces numerical difficulties. An effective approach is to use the capillary potential gradient to express the total velocity, therefore the saturation discontinuity from the contrast in capillary pressure between the rock bulk and discrete fractures can be described (Hoteit and Firoozabadi 2008a, b). However, the common issues in numerical methods of fractured reservoir are numerical robustness and efficiency when heterogeneity and fractured networks are considered, which also consist of the topic of the presented work.

In practice, there are many multiple length fractures in the fractured reservoir. It is impossible to explicitly simulate all of these fractures in a simulation. The limitations are the expensive computational cost and mesh partition of the complex geometry. To this end, we introduce the hierarchical modeling approach (Lee et al. 2001; Khoei et al. 2015; Islam and Manzocchi 2019) to upscale the fine-scale fractures. An equivalent continuum approach is introduced to compute equivalent tensor. Therefore, the effect of fine-scale fractures is reflected by the equivalent tensor, while the large-scale fractures are retained and allowed to be modeled explicitly. The equivalent tensor can be calculated either by the analytical approach (Oda 1985; Hosseini and Khazaei 2021) or flow-based upscaling approach (Islam and Manzocchi 2019). The flow-based upscaling approach is directly derived from the Darcy's law. Oda's method is a widely used approach for a porous medium containing a large number of short fractures (Khoei et al. 2015; Ghahfarokhi 2017), where the equivalent permeability tensor is computed based on the assumption that the fractures are uniformly distributed inside the domain. As a result, the fractured medium is considered as an anisotropic homogeneous medium (Oda 1985; Khoei et al. 2015). In this work, this equivalent continuum approach is integrated in the numerical scheme.

This study focuses on numerical investigation of two-phase flow in fractured porous media. Based on this method, the effects of heterogeneity and fracture distribution on hydraulic characteristics are analyzed. The rest of this paper is organized as follows. First, the formulation of two-phase flow in fractured porous media is provided in Section 2. Then, numerical method is introduced in Section 3. Later, the solution strategy with multilevel adaptive implicit scheme is presented in Section 4. Oda's approach is employed for upscaling the fine-scale fractures. Finally, a number of numerical tests is conducted to study two-phase flow in different patterns of porous media, especially the effects of heterogeneity and fracture distribution are studied.

2 Mathematical Formulation

In this section, the formulation of fluid flow in fractured porous media is provided. The physical domain is modeled by the discrete fracture model (DFM). In the framework of continuum mechanics, fluid flow is governed by the mass conservation and momentum balance (Eymard et al. 2000; Aziz 1979; LeVeque 1992).

2.1 The Model of Fractured Porous Media

In practice, the natural fractures are randomly distributed in porous media. The discrete fractures are considered as the discontinuous interfaces.

Assuming a set of stochastic fractures $\omega = \cup_{i=1}^{N^f} \omega_i$ distributed in a porous medium Ω, each fracture is modeled explicitly. N^f is the number of fractures. The rock matrix is represented by Ω^m.

Figure. 1 illustrates several fractures connected to each other, therefore they create a fracture network. Consequently, the entire domain Ω consists of two main components $\Omega = \Omega^m \cup \omega$. The distribution pattern of the stochastic fractures has great impact on the properties of DFM. There are several representative patterns, typically the orthogonal, parallel and random patterns.

The boundary Γ of this domain is decomposed as Dirichlet type Γ^D and Neumann type Γ^N. Note that $\Gamma = \Gamma^D \cup \Gamma^N$ and $\Gamma^D \cap \Gamma^N = \emptyset$. Consequently, a hybrid-dimensional model is constructed, which implies that the fractures satisfy $\omega \subseteq \mathbb{R}^{n-1}$ and the matrix satisfies $\Omega^m \subseteq \mathbb{R}^n$.

2.2 Governing Equations of Flow and Transport

The formulation of the incompressible and immiscible fluid flow in porous media is given as follows for completeness. For the phase α and phase β, the mobilities are denoted as λ_α and λ_β, respectively. The total mobility is $\lambda_t = \lambda_\alpha + \lambda_\beta$ (Aziz 1979; Dietrich et al. 2005; Eymard et al. 2000). Therefore, the total velocity $\mathbf{u}(p)$ depends on pressure p and is calculated by Darcy's law $\mathbf{u}(p) = -\lambda_t \nabla p$.

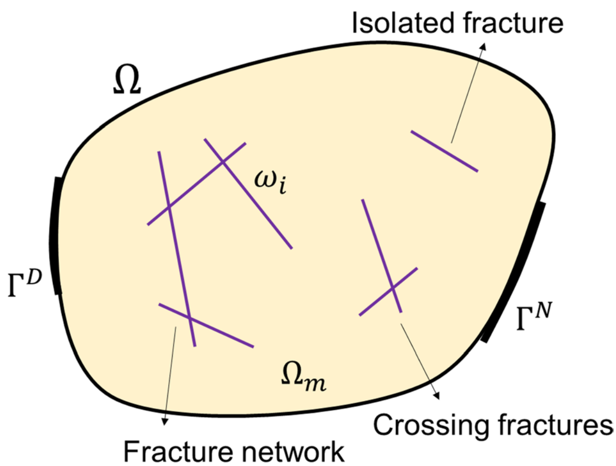

Fig. 1 Schematic of the discrete fracture model (DFM)

Following the hyperbolic conservation laws (LeVeque 1992; Eymard et al. 2000), the conserved quantity $c(\mathbf{x}, t)$, the source term $f(\mathbf{x}, t)$ and the flux $\mathbf{F}(\mathbf{x}, t)$ are functions of an arbitrary temporal-spatial position $(\mathbf{x}, t)$ inside the domain Ω. The general conservation law reads:

$$c_t(\mathbf{x}, t) + \nabla \cdot \mathbf{F}(\mathbf{x}, t) = f(\mathbf{x}, t) \quad \text{on } \Omega \tag{1}$$

The saturation S_α for phase α is introduced according to the theory of two-phase flow (Aziz 1979; Sahimi 2011; Dietrich et al. 2005; Hoteit and Firoozabadi 2008b). For a porous medium with porosity ϕ and volumetric flux q, the two terms in Eq. (1) are expressed as $\mathbf{F}(\mathbf{x}, t) = f_\alpha\left(S_\alpha\right)\mathbf{u}(p)$ and $f(\mathbf{x}, t) = f_\alpha\left(S_\alpha\right)q$, respectively. The fractional flow $f_\alpha\left(S_\alpha\right)$ is a nonlinear function, defined as $f_\alpha\left(S_\alpha\right) = \lambda_\alpha\left(S_\alpha\right)/\lambda_t$ (Aziz 1979; Eymard et al. 2000; Dietrich et al. 2005).

Consequently, the transport equation for incompressible and immiscible fluid is derived from Eq. (1). To summarize, the governing equations for fluid flow and transport read:

$$\begin{aligned} -\nabla \cdot \left[\lambda_t \nabla p\right] &= q \quad \text{on } \Omega \times T(0, t) \\ \phi \frac{\partial S_\alpha}{\partial t} + \nabla \cdot \left[f_\alpha\left(S_\alpha\right)\mathbf{u}(p)\right] &= f_\alpha\left(S_\alpha\right)q \quad \text{on } \Omega \times T(0, t) \end{aligned} \tag{2}$$

where the domain of entire time is $T(0, t)$.

Eq. (2) constructs a coupled system of nonlinear elliptic-hyperbolic (PDEs). As shown in Fig. 1, both the Dirichlet and Neumann types can be applied on Γ^D and Γ^N, respectively. The initial condition is pre-defined at the initial time $T(0)$. For all fractures and matrix, it reads:

$$\begin{aligned} p_\alpha &= \bar{p} \quad \text{on } \Gamma^D \times T\left(0, t_n\right) \\ -\left(\lambda_t \nabla p\right) \cdot \mathbf{n} &= \bar{q} \quad \text{on } \Gamma^N \times T\left(0, t_n\right) \\ S_\alpha &= \bar{S}_\alpha \quad \text{on } \Omega \times T(0) \end{aligned} \tag{3}$$

where $\mathbf{n}$ is the outward unit vector to the external boundary. $\bar{p}$, $\bar{q}$ and $\bar{S}_\alpha$ are the pre-defined quantities. The unknown for phase β is $S_\beta = 1 - S_\alpha$.

3 Numerical Method

In this section, the system of PDEs, i.e. Eqs. (2) and (3), is discretized based on the finite element formulation with Euler Backward scheme (implicit) and the upwind algorithm.

3.1 The Unstructured Grids on DFM

The Delaunay triangulation (Shewchuk 2002) is used to generate the unstructured grids by triangular cells, as illustrated in Figure. 2. The fractures are partitioned by a set of finite low-dimensional cells ω^{ele}, while the matrix is partitioned by the high-dimensional cells Ω^{ele}. Therefore, we have $\omega^{ele} \subseteq \mathbb{R}^{n-1}$ and $\Omega^{ele} \subseteq \mathbb{R}^n$.

Therefore, the physical domain Ω is partitioned by the generated unstructured grids:

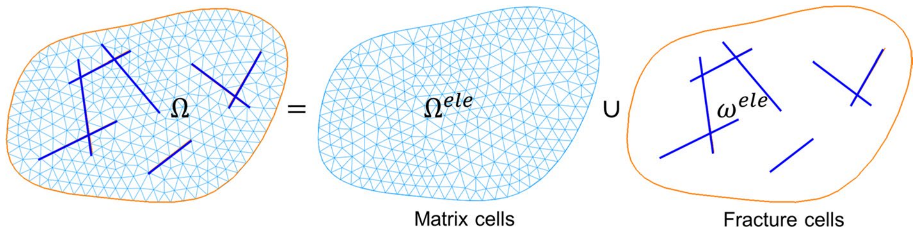

Fig. 2 Delaunay triangulation. The unstructured grids are composed of the high-dimensional cells Ω^{ele} and the low-dimensional cells ω^{ele}

$$\Omega = \left(\cup_{i=1}^{n^m} \Omega_i^{ele}\right) \cup \left(\cup_{j=1}^{n^f} \omega_j^{ele}\right) \tag{4}$$

where n^m and n^f are the numbers of matrix and fracture cells, respectively. The governing equations in Eq. (2) are valid on each of the partitioned cells (Wang et al. 2022).

3.2 Numerical Discretization

Following the framework of the Galerkin finite element method (GFEM) (Wang 2003; Zienkiewicz et al. 2013; Borst 2018), the temporal and spatial integrals are applied over a time interval Δt and the domain Ω. We consider the integrals of the governing equation Eq. (2):

$$\begin{aligned} &\int_\Omega -\nabla \cdot \left[\lambda_t \nabla p\right] dV = \int_\Omega q dV \\ &\int_{\Delta t}\int_\Omega \phi \frac{\partial S_\alpha}{\partial t} dV dt + \int_{\Delta t}\int_\Omega \nabla \cdot \left[f_\alpha\left(S_\alpha\right)\mathbf{u}(p)\right] dV dt = \int_{\Delta t}\int_\Omega f_\alpha\left(S_\alpha\right) q dV dt \end{aligned} \tag{5}$$

where the time-dependent term $\phi\left(\partial S_\alpha / \partial t\right)$ is discretized by Euler Backward difference scheme (implicit):

$$\underbrace{\int_\Omega \frac{\phi}{\Delta t}\left(S_\alpha^{n+1} - S_\alpha^n\right) dV}_{\text{Time-dependent term}} + \underbrace{\int_\Omega \nabla \cdot \left[f_\alpha\left(S_\alpha\right)\mathbf{u}(p)\right]^{n+1} dV}_{\text{Flux term}} = \underbrace{\int_\Omega \left[f_\alpha\left(S_\alpha\right) q\right]^{n+1} dV}_{\text{Source term}} \tag{6}$$

The primary unknown of Eq. (6) is saturation S_α. It should be noted that the term $\left[f_\alpha\left(S_\alpha\right)\mathbf{u}(p)\right]^{n+1}$ is related to the unknown pressure p, which is coupled through velocity $\mathbf{u}(p)$. Applying the Gauss theorem to the first equation in Eq. (5) and Eq. (6), the semi-discretized forms hold true on each cell Ω_i^{ele}:

$$\sum_{i=1}^{n^{all}} \int_{\partial\Omega_i^{ele}} -\left[\lambda_t \nabla p\right]^{n+1} \cdot \mathbf{n} d\Gamma = \int_{\Omega_i^{ele}} q^{n+1} dV \tag{7}$$

and

$$\sum_{i=1}^{n^{all}} \int_{\Omega_i^{ele}} \frac{\phi}{\Delta t}\left(S_\alpha^{n+1} - S_\alpha^n\right) dV + \sum_{i=1}^{n^{all}} \int_{\partial\Omega_i^{ele}} \left[f_\alpha\left(S_\alpha\right)\mathbf{u}(p)\right]^{n+1} \cdot \mathbf{n} d\Gamma = \sum_{i=1}^{n^{all}} \int_{\Omega_i^{ele}} \left[f_\alpha\left(S_\alpha\right) q\right]^{n+1} dV \tag{8}$$

with the number of all cells $n^{all} = n^m + n^f$. Note that the symbol of cell Ω_i^{ele} can be either a fracture cell or matrix cell. In this way, pressure and saturation are coupled through the coupled terms λ_t and $f_\alpha\left(S_\alpha\right)$, which should be updated at each time step during iteration.

The unknowns p and S_α (for convenience $S_\alpha = S$) are solved by the finite element scheme (Jha and Juanes 2007). The approximations are given based on GFEM (Jha and Juanes 2007; Zienkiewicz et al. 2013), $p \approx p_h = \sum_{i=1}^{n^{all}} \eta_i p_i$ and $S \approx S_h = \sum_{i=1}^{n^{all}} \xi_i S_i$. η and ξ are the shape functions.

As shown in Fig. 3, a certain cell Ω_i^{ele} has n_i^{neig} edges connecting to its neighbors Ω_j^{ele}, Ω_k^{ele} and Ω_m^{ele}, etc. The boundary $\partial\Omega_i^{ele}$ is decomposed by its sub-edges σ_{i*}. Therefore, we have $\partial\Omega_i^{ele} = \cup_{*=j,k,m,\ldots}^{n_i^{neig}} \sigma_{i*}$.

The semi-discretized forms Eqs. (7) and (8) are rewritten as:

$$\sum_{*=j,k,m,\ldots}^{n_i^{neig}} \int_{\sigma_{i*}} -\left[\lambda_t \nabla(\eta p)\right]^{n+1} \cdot \mathbf{n}_{\boldsymbol{\sigma}_{\mathbf{i}*}} d\Gamma = \int_{\Omega_i^{ele}} q^{n+1} dV \tag{9}$$

and

$$\int_{\Omega_i^{ele}} \frac{\phi}{\Delta t} \xi\left(S^{n+1} - S^n\right) dV + \sum_{*=j,k,m,\ldots}^{n_i^{neig}} \int_{\sigma_{i*}} \left[f(S)\mathbf{u}(p)\right]^{n+1} \cdot \mathbf{n}_{\boldsymbol{\sigma}_{\mathbf{i}*}} d\Gamma = \int_{\Omega_i^{ele}} \left[f(S)q\right]^{n+1} dV \tag{10}$$

The fully discretized forms are given in Appendix A. Besides, the flux term shown in Eq. (6) is discretized by the upwind algorithm. We refer to Appendix B for the detail.

4 Solution Strategy

In this section, the two primary unknowns, p and S, are solved using an iterative method (Aziz 1979; Wesseling 2001). A multilevel adaptive implicit scheme is devised to improve the numerical robustness and efficiency. Then, an equivalent continuum

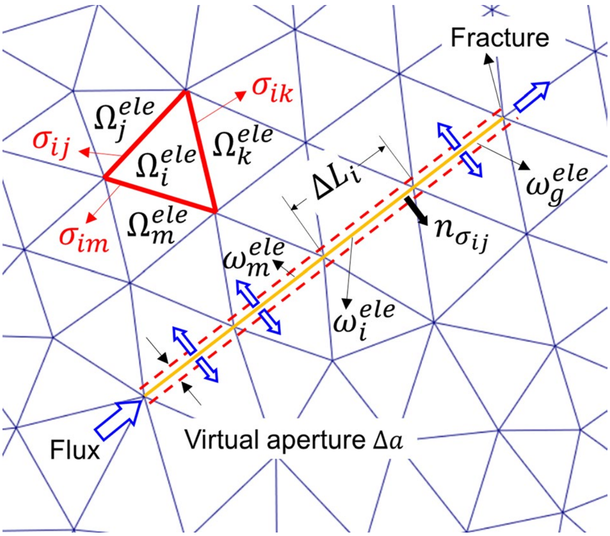

Fig. 3 Key parameters of fracture and matrix cells

approach is introduced to upscale the fine-scale fractures. All algorithms have been implemented in our C++ program (Wang et al. 2022).

4.1 Implicit Iteration

To solve the system of Eqs. (9) and (10) by an iterative method, the nonlinear residuals are expressed as:

$$\left[R_i^m\right]^{n+1} = \left[f_i q_i\right]^{n+1} \Delta V_i - \frac{\phi \Delta V_i \xi_i}{\Delta t}\left(S_i^{n+1} - S_i^n\right) \quad - \sum_{*=j,k,m,\dots}^{n_i^{neig}} \left[f_\uparrow \, \mathbf{u}_{i*}\right]^{n+1} \Delta A_{i*} \tag{11}$$

for matrix cells, and:

$$\left[R_i^f\right]^{n+1} = \left[f_i q_i\right]^{n+1} \Delta L_i \Delta a_i - \frac{\phi \Delta L_i \Delta a_i \xi_i}{\Delta t}\left(S_i^{n+1} - S_i^n\right) \quad - \sum_{*=j,k,m,\dots}^{n_i^{neig}} \left[f_\uparrow \, \mathbf{u}_{i*}\right]^{n+1} \Delta l_{i*} \tag{12}$$

for fracture cells. As shown in Fig. 3, ΔL_i and Δa_i are the length and aperture of a fracture cell, respectively. Δl_{i*} in Eq. (12) is determined by the velocity on its corresponding interface, as indicated in the upwind algorithm (Appendix B). If the velocity is of fracture-fracture, $\Delta l_{i*} = \Delta a_i$; if the velocity is of matrix-fracture, $\Delta l_{i*} = \Delta L_i$.

The residual vector is defined for all cells, $\mathbf{R} = \left[\mathbf{R}^m \;\; \mathbf{R}^f\right]^T$. Note that the superscripts m and f are the matrix and fracture, respectively. At a certain iteration step ν, the Jacobian is constructed using the derivative of the residual vector:

$$\mathbf{J}^\nu = \left.\frac{\partial \mathbf{R}}{\partial \mathbf{S}}\right|^\nu \tag{13}$$

with the saturation vector $\mathbf{S} = \left[\mathbf{S}^m \;\; \mathbf{S}^f\right]^T$.

The incremental form of Newton-Raphson iteration is $\mathbf{J}^\nu \delta \mathbf{S}^{\nu+1} = -\mathbf{R}^\nu$. Therefore, the value of $\mathbf{S}$ at iteration step $\nu + 1$ is updated by $\mathbf{S}^{\nu+1} = \mathbf{S}^\nu + \delta \mathbf{S}^{\nu+1}$.

The solution strategy in this work is to split the global solution of p and S into two blocks and then to solve them iteratively (Aziz 1979; Wesseling 2001). p^{n+1} is calculated from Eq. (9) at time $n + 1$, then enter the procedure to solve S^{n+1} by Eqs. (11), (12) and (13). The algebraic system for iteration is assembled into one block and rewritten as:

$$\begin{bmatrix} \mathbf{J}^{mm} & \mathbf{J}^{mf} \\ \mathbf{J}^{fm} & \mathbf{J}^{ff} \end{bmatrix} \begin{bmatrix} \delta \mathbf{S}^m \\ \delta \mathbf{S}^f \end{bmatrix} = - \begin{bmatrix} \mathbf{R}^m \\ \mathbf{R}^f \end{bmatrix} \tag{14}$$

The discretized form of the algebraic system is given in Appendix C. Fig. 4 shows the flowchart of the solution strategy. The nonlinear convergence of the iteration is reached once the criterion is satisfied.

4.2 Multilevel Adaptive Time-Stepping Strategy

The time increment Δt controls the advance of time step in this iteration. Furthermore, the convergence performance of the numerical scheme is also significantly influenced by Δt. The convergence criterion is given by:

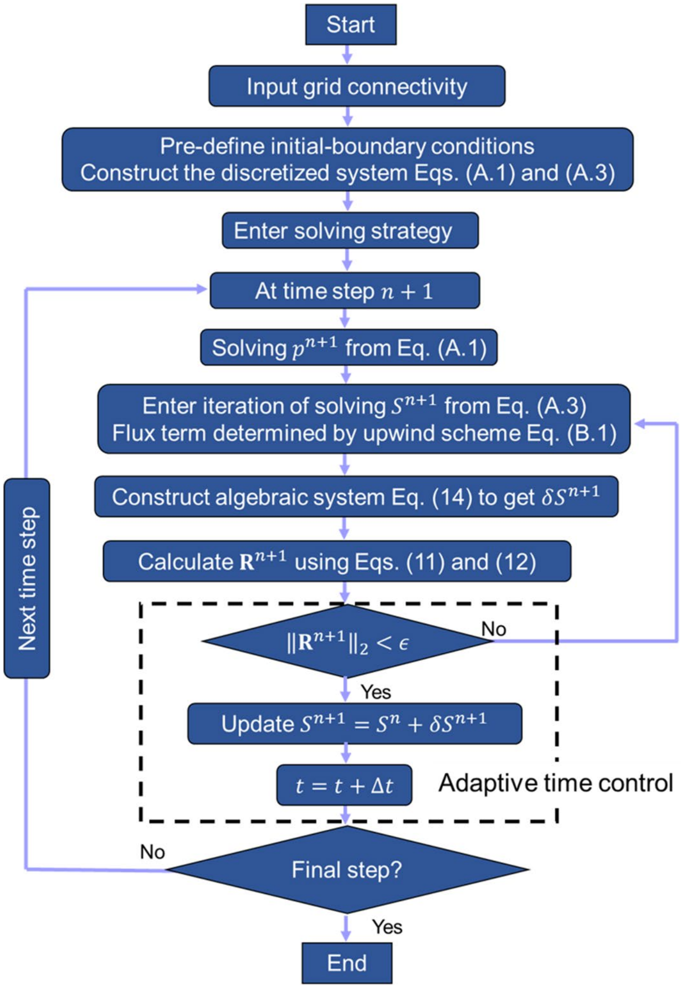

Fig. 4 Flowchart of the solution strategy. The steps highlighted by the dashed box are shown in Algorithm 1

$$\left\|\mathbf{R}^{n+1}\right\|_2 < \epsilon \tag{15}$$

with the user-defined threshold ϵ.

The L^2 norm of residual $\left\|\mathbf{R}^{n+1}\right\|_2$ is affected by Δt. An appropriate Δt enables a low cost iteration as well as a good convergence performance. The optimal option is to set a variable Δt which can be updated dynamically during the iteration (Alikhani et al. 2016; Shepherd et al. 2019). The procedure of adaptive time step control is shown in Algorithm 1.

The literature shows that there are two representative strategies, namely the sequential implicit (SI) strategy (Sheth and Younis 2017) and the fully implicit (FI) strategy (Ganis et al. 2014). Both of them have been widely applied in reservoir simulation. The computational cost of SI is relatively lower than the FI, since the size of algebraic system in SI is smaller than that of in FI. Obviously, a matrix with a larger size may induce a more ill-condition Jacobian. Moreover, the convergence criterion in FI is more stricter than that of in SI, where one needs to handle both the residual of p and S in FI, but in SI one just considers the residual of S. Therefore, the implementation of adaptive strategy in SI is more convenient that of in FI. To balance the pros and cons, we use the sequential implicit strategy in this study.

As shown in Fig. 4, the adaptive iteration is applied if the steps highlighted by dashed box are replaced by the Algorithm 1. Otherwise, the fixed time step is used. Note that W_1 and $Y_i, (i = 1, 2)$ are the user-defined factors to measure convergence condition. w_i and y_i are factors to update Δt^*. A feasible optional in the implementation is to set $W_1 = 10^2$, $w_1 = 1/5, w_2 = 1/2$; $Y_1 = 10^{-3}, Y_2 = 10^{-2}$ and $y_1 = 5, y_2 = 2$. Different adaptive strategies and the classical method will be studied and compared in Section 5.

Algorithm 1 Procedure of the multilevel adaptive scheme

Note that t_T is the maximum time step
Define $W_1 > 1$, $0 < w_1 < w_2 < 1$; $0 < Y_1 < Y_2 < 1$ and $y_1 > y_2 > 1$ with $i = 1, 2$

for each time step $t \in [1, t_T]$ **do**
  Solve p^{n+1} and δS^{n+1}
  Calculate L^2 norm of residual $\|\mathbf{R}^{n+1}\|_2$
  if $\|\mathbf{R}^{n+1}\|_2 < \epsilon$ **then**
    Update S^{n+1}
  else if $\|\mathbf{R}^{n+1}\|_2 > W_1 \times \epsilon$ **then**
    $\Delta t^* = w_1 \times \Delta t$; move to the next iteration
  else
    $\Delta t^* = w_2 \times \Delta t$; move to the next iteration
  end if
  Enter the adaption of the next time step
  if $\|\mathbf{R}^{n+1}\|_2 < Y_1 \times \epsilon$ **then**
    $\Delta t^* = y_1 \times \Delta t$
  else if $\|\mathbf{R}^{n+1}\|_2 < Y_2 \times \epsilon$ **then**
    $\Delta t^* = y_2 \times \Delta t$
  else
    $\Delta t^* = \Delta t$
  end if
  Update $t = t + \Delta t^*$
end for

4.3 Oda's Method of Permeability Tensor

A hierarchical modeling approach is introduced to simplify geometrical complexity and to reduce computational cost. In this study, Oda's method is used to upscale a fractured medium with uniformly distributed small size fractures (Oda 1985; Khoei et al. 2015; Ghahfarokhi 2017), while the large size fractures are retained and allowed to be explicitly modeled.

Oda's method is a widely used upscaling approach for calculating permeability tensor (Oda 1985). Here we apply it to two-phase flow in fractured media (Khoei et al. 2015). For a sub-domain with volume V_{sub}, the mean velocity of phase α is expressed as:

$$\bar{\mathbf{u}}_\alpha = \frac{1}{V_{sub}}\left(\int_{V_{sub,m}} \frac{k_{r\alpha}}{\mu_\alpha}\mathbf{k}_m \nabla p\, dV + \sum_{i=1}^{N^f}\int_{V^i_{sub,f}} \bar{\mathbf{u}}^f_{\alpha,i}\, dV\right) \tag{16}$$

where the volumes of matrix and fractures in the sub-domain are $V_{sub,m}$ and $V_{sub,f}$, respectively. μ_α and $k_{r\alpha}$ are viscosity and relative permeability of phase α. The mean velocity $\bar{\mathbf{u}}^f_\alpha$ in fracture i follows the cubic law and reads (Khoei et al. 2015):

$$\bar{\mathbf{u}}^f_{\alpha,i} = \frac{k_{r\alpha}}{\mu_\alpha} \frac{\Delta a_i^2}{12} \left[\nabla p - \left(\mathbf{n}_i^f \cdot \nabla p \right) \mathbf{n}_i^f \right] \tag{17}$$

where $\mathbf{n}_i^f$ is the unit vector normal to fracture i.

Therefore, the equivalent permeability tensor $\mathbf{k}_{eq}$ of this sub-domain is derived as:

$$\mathbf{k}_{eq} = \mathbf{k}_m + \sum_{i=1}^{N_f} \mathbf{k}_f^i \tag{18}$$

The permeability of fracture i is written as:

$$\mathbf{k}_f^i = \frac{1}{V_{sub}} \frac{\Delta a_i^3 \Delta L_i}{12} \left(\mathbf{I} - \mathbf{n}_i^f \otimes \mathbf{n}_i^f \right) \tag{19}$$

where $\mathbf{I}$ is the identity tensor. $\otimes$ is the outer product of tensors. Other notations are defined in the preceding sections.

Note that Eq. (18) holds in a fractured medium with uniformly distributed small fractures. In Section 5, we will apply Eq. (18) to upscale the fine-scale fractures.

5 Numerical Results and Discussion

Numerical studies are performed in this section using the modeling approach proposed in Sections 3 and 4. First, the presented numerical scheme is verified by a benchmark study. The robustness and efficiency of the scheme are demonstrated under different conditions. Then, numerical tests are performed to analyze the effects of heterogeneity, multiple length fractures and fracture distribution on fluid flow in fractured porous media.

5.1 Numerical Validation and Performance Evaluation

Numerical test is conducted to verify our method and to evaluate the convergence performance, then different adaptive schemes are selected and a comparison study demonstrates the numerical robustness and efficiency of this scheme.

The crossing-fractures model is shown in Fig. 5. It is a widely used benchmark model in fluid flow simulation (Hajibeygi et al. 2011; Tene et al. 2017). The coordinates of fracture are shown in this figure. The size of the domain is 9m × 9m. The injection is placed at the left bottom corner (1 MPa), while the outlet is placed at the right top corner. Permeability of the rock bulk is $k_m = 1 \times 10^{-12}\mathrm{m}^2$. Fracture permeability is $k_f = 1 \times 10^{-7}$ and $1 \times 10^{-17}\mathrm{m}^2$. Thereafter, we define the permeability ratio $k_r = k_f / k_m$ to measure the conductivity of this medium.

The simulation results are displayed in Fig. 5. It appears that the permeability ratio has strong effect on fluid flow. Saturation profile is illustrated in different pore volume injection (PVI). The high permeability ratio ($k_r = 10^5$) leads to a conductive channel for flow, while a small permeability ratio ($k_r = 10^{-5}$) produces a barrier effect.

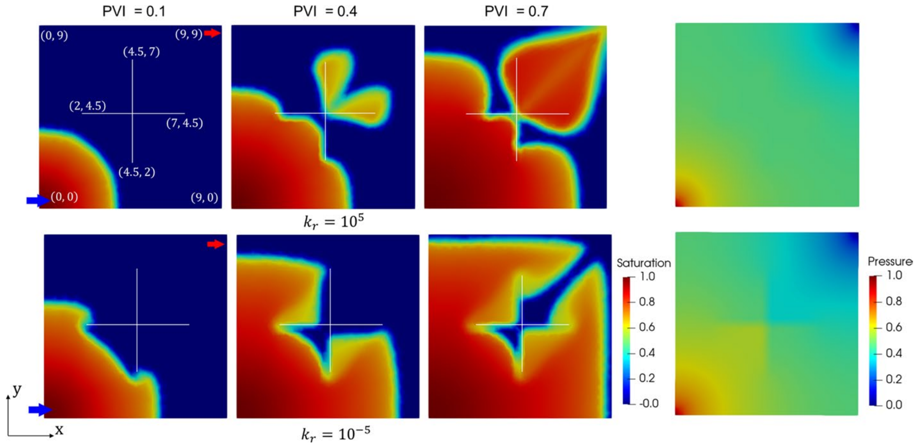

Fig. 5 The crossing-fractures model. Saturation evolution and pressure distribution of the fractured medium with different permeability ratio k_r

To evaluate the performance of the multilevel adaptive time (AT) scheme, different strategies are selected, as shown in Table 1. The convergence factors and adaptive factors are defined in Algorithm 1. These factors control the adaptive level. We test four different strategies, concerning the 4-levels (AT-4L) and 3-levels (AT-3L). The variation of time step Δt^* during iteration is shown in Fig. 6 (left). To test the performance of the adaptive scheme, a strict convergence criterion is considered ($\epsilon = 5 \times 10^{-10}$). Δt^* will be decreased dramatically if the adaptive scheme is applied, while it keeps a constant if the fixed time (FT) scheme is used. Obviously, the adaption of time step during iteration automatically changes Δt^*, therefore the computational cost will be reduced correspondingly. We use the total number of Newton iteration N_{iter} to represent the cost. The comparison of different schemes is shown in Fig. 6 (right) with different numbers of grids. It implies that the adaptive time scheme improves the computational efficiency compared to the fixed time scheme.

The three-fractures model is displayed in Fig. 8, in which the comparison with reference solution is provided. Following the parameters given by Karimi-Fard et al. (2004), we set $k_m = 0.99 \times 10^{-15}\mathrm{m}^2$ and $k_f = 8.33 \times 10^{-10}\mathrm{m}^2$. It appears that the saturation evolution calculated by the presented method agrees well with the reference solution. Furthermore, Fig. 7 shows the convergence performance of the crossing-fractures model and the three-fractures model during iteration using different strategies. As depicted in this figure, the

Table 1 Parameters of multilevel adaptive time (AT) scheme. Different adaptive strategies with 4-levels (AT-4L) and 3-levels (AT-3L), corresponding to Algorithm 1

Adaptive strategies		AT-4L1	AT-4L2	AT-3L1	AT-3L2
Convergence factor	W_1	10^2	10	10^2	-
	Y_1	10^{-3}	10^{-2}	10^{-2}	10^{-2}
	Y_2	10^{-2}	10^{-1}	–	10^{-1}
Adaptive factor	w_1	1/5	1/2	1/5	–
	w_2	1/2	$1/\sqrt{2}$	1/2	1/2
	y_1	5	2	5	2
	y_2	2	$\sqrt{2}$	–	$\sqrt{2}$

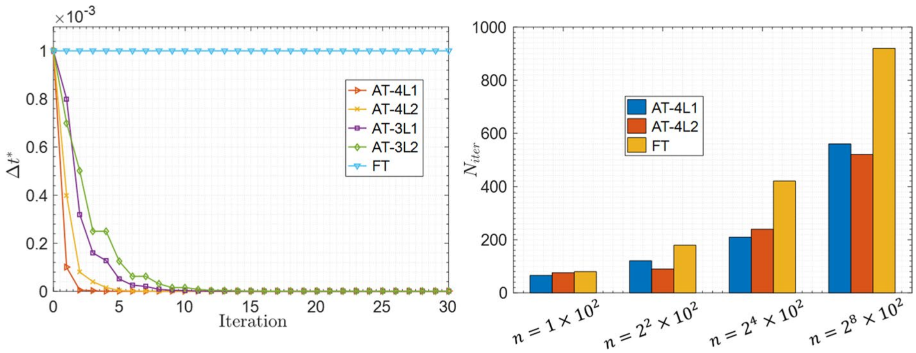

Fig. 6 Variation of time step of the crossing-fractures model using different adaptive strategies (left), when the threshold $\epsilon = 5 \times 10^{-10}$. The total number of Newton iteration versus the number of grids (right)

convergence condition is influenced by the permeability ratio k_r. It indicates that the adaptive time scheme improves the convergence condition compared to the fixed time scheme.

5.2 A Heterogeneous Porous Medium with Layered Permeability

The heterogeneity of permeability has significant effect on fluid flow. To investigate the effect of heterogeneity, a layer model with different layer angles θ is shown in Fig. 9. The size of the domain is $500\text{m} \times 270\text{m}$. The permeability of the rock matrix is assigned as a layered layout, in which the permeability of each layer is set to an alternate pattern (10^{-12} or 10^{-14}m^2).

Three cases (Cases $1 \sim 3$) are analyzed with different angles $\theta = 0°, 45°$ and $90°$, as displayed in Fig. 9. Initial saturation of the model is set to a random pattern, in the range $2.3 \times 10^{-2} \sim 1.7 \times 10^{-1}$. The pre-given pressure 1 MPa is imposed on the left boundary, while the outlet is placed on the right boundary. The physical properties used in simulation are shown in Table 2. Note that the relative permeabilities $k_{r\alpha}$ and $k_{r\beta}$ are determined by the Brooks-Corey relations (Brooks and Corey 1964):

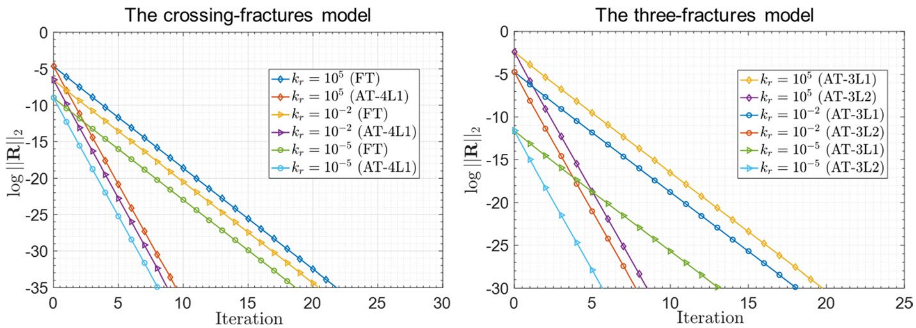

Fig. 7 Convergence history of the crossing-fractures model (left) and the three-fractures model (right) under different conditions

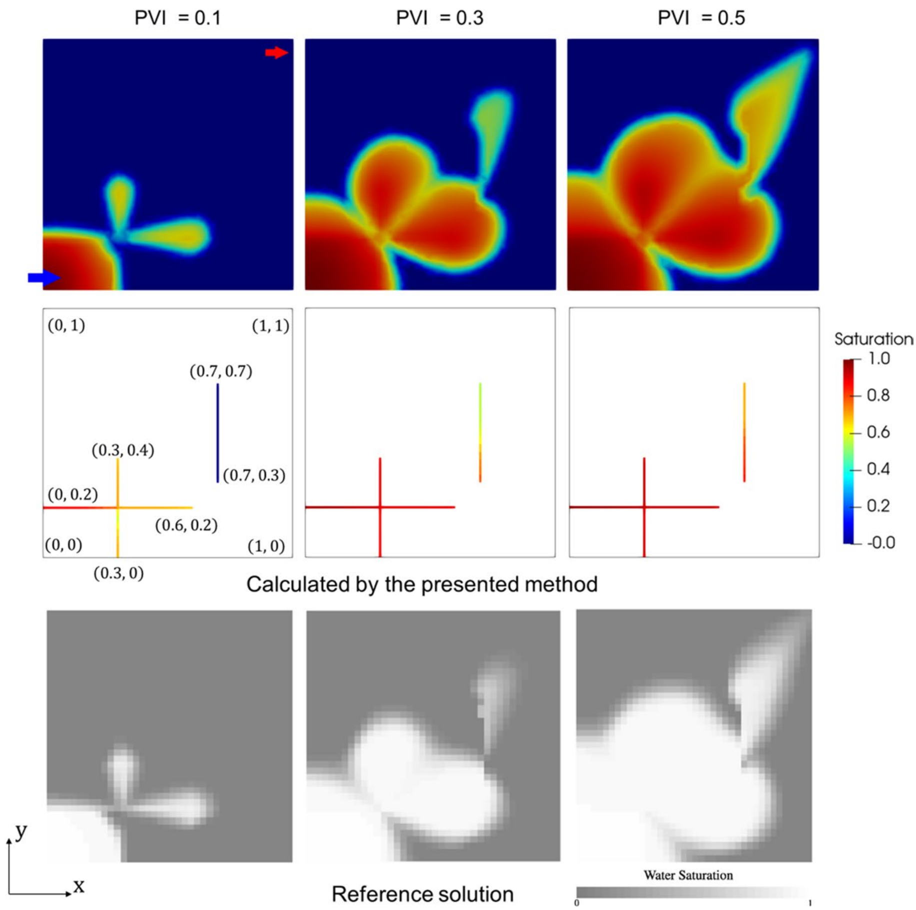

Fig. 8 The three-fractures model. Comparison between the reference solution and the results simulated by the presented method

$$k_{r\alpha} = S_n^2, \quad k_{r\beta} = \left(1 - S_n\right)^2 \tag{20}$$

where the normalized saturation S_n is defined as $(S_\alpha - S_{\alpha l)}/(1 - S_{\alpha l} - S_{\beta l})$. $S_{\alpha l}$ and $S_{\beta l}$ are the irreducible saturation, as given in Table 2.

Simulation results are displayed in Fig. 10. The saturation evolution, as well as pressure field, is strongly influenced by the layer angle. The layers with a relatively low permeability (10^{-14}m^2) show the barrier effect in Case 1 ($\theta = 0°$). In contrast, the layers with a high permeability (10^{-12}m^2) provide a conductive channel for fluid flow. In Case 2, the direction of fluid flow follows the layer orientation. The effect of barrier effect gradually decreases with the increase of angle. Therefore, the saturation profile appears an uniform pattern in Case 3 ($\theta = 90°$). The linear pressure gradient is observed in Cases 1 and 3, while it shows a different pattern in Case 2.

It appears that different layer angles may change the pattern of fluid flow as well as the production. Fig. 12 illustrates the relation of pore volume injection versus pore volume production. We compare two different situations, the uniform and random initial

Table 2 Physical properties in simulation

Physical properties	Values	Units
Matrix permeability k_m	1×10^{-12}	m^2
Fracture permeability k_f	$1 \times 10^{-17} \sim 1 \times 10^{-7}$	m^2
Fracture aperture a^f	0.1	mm
Fracture porosity ϕ_f	1	-
Matrix porosity ϕ_m	0.2	-
Relative permeability	Brooks-Corey relations	-
Irreducible saturation $S_{\alpha l}$	0.001	-
Irreducible saturation $S_{\beta l}$	0	-
Dynamic viscosity of phases α	0.001	$Pa \cdot s$
Dynamic viscosity of phases β	5×10^{-4}	$Pa \cdot s$

saturation S_{ini}, in Cases 1 ~ 3. Simulation results imply that the layer angle influences the pore volume production. The model in Case 3 produces a relatively high production due to the high efficiency of driving fluid, while the production in Case 1 is relatively low compared to other cases. The reason is that the layers are set to the direction of flow and then directly conduct the injected fluid to the outlet. Moreover, it is observed that the random S_{ini} has a slight influence on production, since the domain is partially filled with initial saturation before injection.

In contrast to the layer model, a porous medium with a fracture network (Case 4) is simulated with a random permeability field. Figure. 11 shows the permeability distribution and saturation evolution. The range of k_m is $6 \times 10^{-11} \sim 1 \times 10^{-9}$ m^2. Note that k_r is determined by $k_f / \min(k_m)$ since k_m is random. It can be seen from this figure that the fracture network provides a dominant channel for fluid flow. We compare the pore volume production of the fracture network model (Case 4) with different permeability ratio k_r and different permeability field (uniform or random k_m), as shown in Figure. 13. It appears that a large k_r would lead to a relatively high production compared to a small k_r. The reason is that the fracture network plays the role of barrier in the later case, therefore the injected fluid is blocked around fractures.

Apparently, the layer model and the fracture network model show different flow patterns. To study the difference between them, the pressure and saturation distributions along a survey line, which is placed at the middle of horizontal direction in models, are depicted in Figure. 14. Pressure distribution of Cases 1 ~ 4 is displayed in the left top inset of this figure. It appears that the variation range of pressure in Case 2 is relatively larger than other cases, since the effect of layer angle plays a dominant role. Saturation evolution along the survey line displays an oscillation in Cases 1 and 2, while it shows a smooth shape in Case 3. Furthermore, the results reveal the effect of layer angle and heterogeneity on fluid flow. The existence of fracture network in Case 4 influences the saturation distribution along the survey line, where a discontinuity produced by the fractures is observed.

The performance of adaptive scheme depends on the adaptive factors, as shown in Table 1. We test different adaptive schemes to compare their computational efficiency. The simulation results are displayed in Fig. 15. The 4-levels, 3-levels schemes and the classical fixed time scheme are applied to simulate Cases 1 ~ 4. Figure. 15 (left) provides the bar graphs for comparison of the number of total Newton iteration. It proves that the adaptive scheme is better than the fixed scheme. However, the computational cost of different

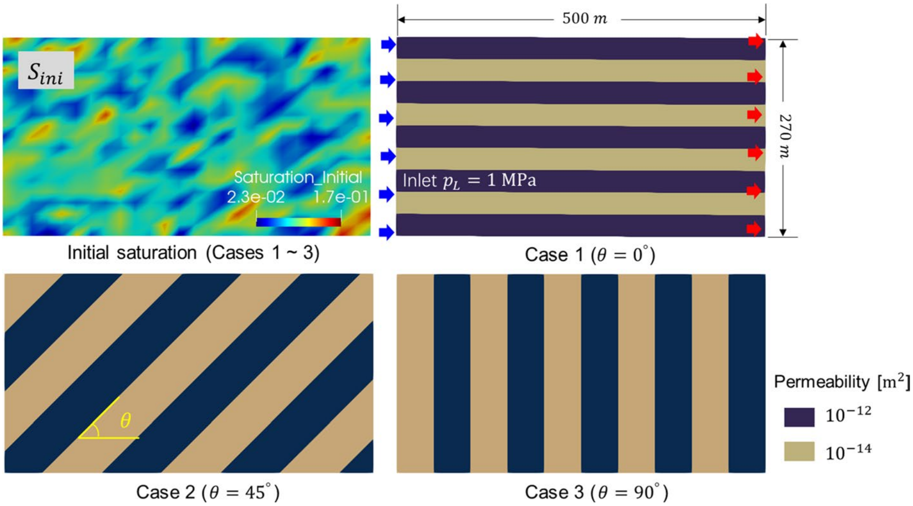

Fig. 9 The layer model with heterogeneity (Cases 1 ~ 3). The initial saturation and the layered permeabilities

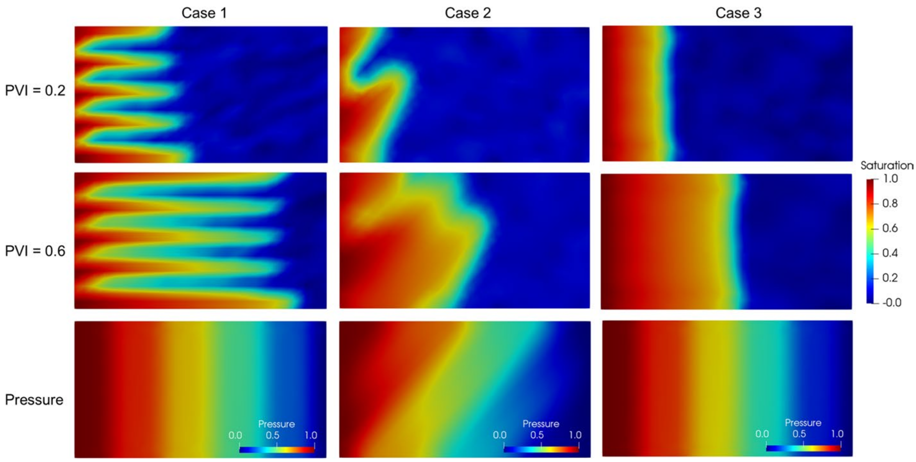

Fig. 10 Saturation evolution (top and middle) and pressure distribution (bottom) of the layer model with heterogeneity (Cases 1 ~ 3) corresponded to Fig. 9

adaptive schemes is related to the adaptive factors. In this context, the AT-4L1 scheme enjoys a relatively high efficiency. Figure. 15 (right) shows the variation of time step during iteration in Case 4. The threshold of convergence criterion is set to 5×10^{-6}. It is observed that a low permeability of fractures improves the convergence condition. The cause might be that the fractures are barriers such that the fracture cells do not involved in computation compared to the conductive matrix cells.

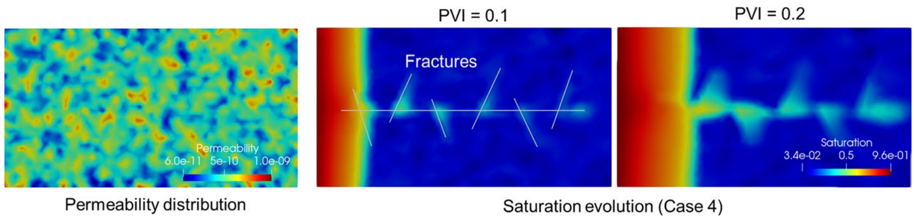

Fig. 11 Permeability distribution and saturation evolution of Case 4 with a fracture network

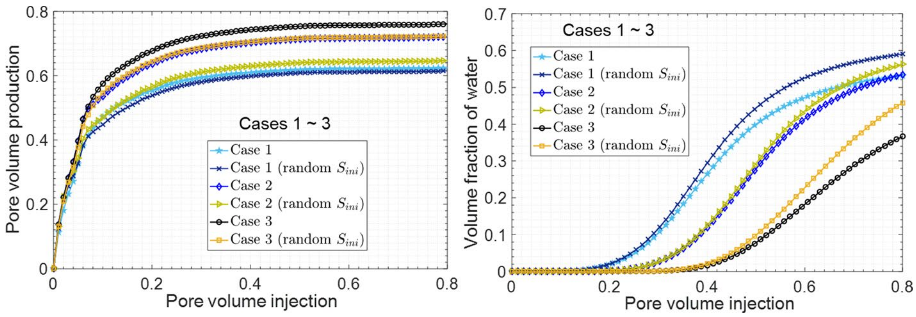

Fig. 12 The layer model (Cases 1 ~ 3). Curves of pore volume injection (PVI) versus pore volume production (left) and PVI versus volume fraction of water (right)

5.3 A Fractured Porous Medium with Multiple Length Fractures

In practice, a naturally fractured reservoir contains many multiple length fractures. The distribution and size of fractures may impact fluid flow in the reservoir. However, it is impossible that all of the multiple size fractures are explicitly modeled in simulation, since the limitations of complicated geometry and expensive computational cost. In this section, we use a hierarchical approach to model the fine-scale and large-scale fractures separately.

Figure. 16 shows the geometry of a fractured reservoir. The size of the domain is 500m × 500m. The fine-scale fractures consist of two fracture groups, as shown in Table 3. We use the statistical parameters to describe the fracture distribution. Each of the groups contains 1500 fractures, where the orientation and length follow the normal distribution. These fine-scale fractures are upscaled by the Oda's method, as discussed in Section 4.3. The domain is partitioned into 15 × 15 sub-squares for calculation of the equivalent permeability tensor. We compute the average value of each component in the tensor. Finally, the components of permeability tensor are $k_{xx} = 6.5 \times 10^{-11}\mathrm{m}^2$, $k_{yy} = 6.9 \times 10^{-11}\mathrm{m}^2$ and $k_{xy} = -1.2 \times 10^{-12}\mathrm{m}^2$. There are five large-scale fractures placed at the center of the domain, as illustrated in Figure. 16. The injection consists of nine spots (10 MPa) along the four sides of the domain. The outlet is located at the middle of the horizontal fracture. The physical properties used in the simulation are shown in Table 2.

In addition, we consider the middle-scale fractures distributed inside the reservoir, which are modeled explicitly in this simulation. Three different angles $\theta = 0°, 45°$ and $90°$ of the middle-scale fractures are shown in Fig. 17. Based on this, we analyze the influence of fracture angle on fluid flow and production. Fig. 18 shows the saturation evolution and pressure field in different cases. Note that the permeability ratio is set to $k_r = 10^5$. It is

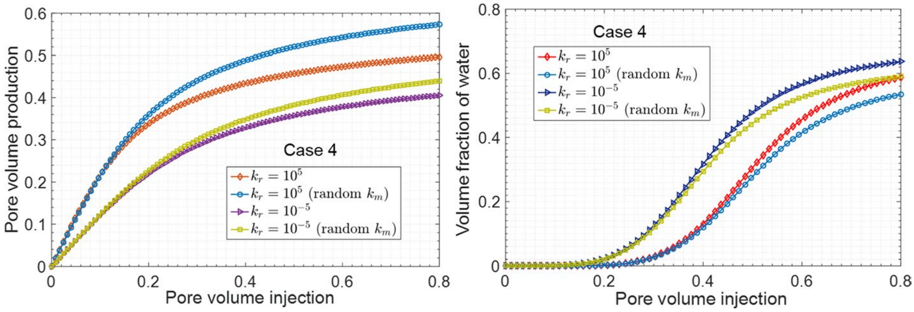

Fig. 13 The fracture network model (Case 4). Curves of pore volume injection (PVI) versus pore volume production (left) and PVI versus volume fraction of water (right)

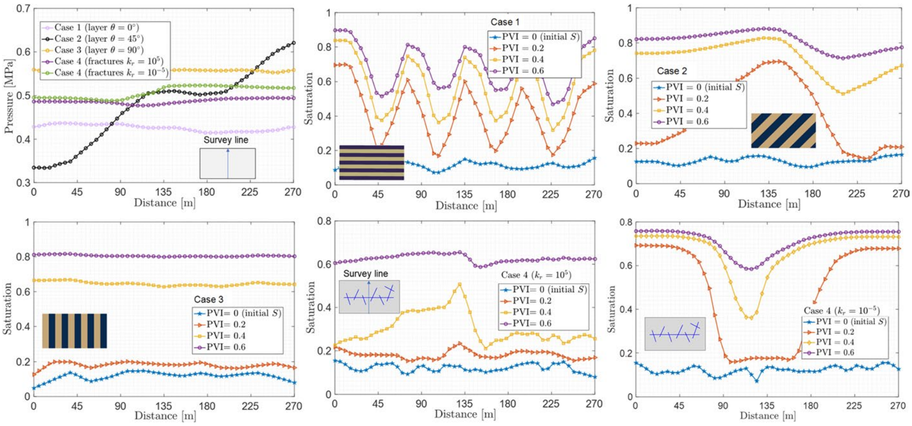

Fig. 14 Pressure distribution and saturation evolution along a survey line. The layer model (Cases 1 ~ 3) and the fracture network model (Case 4)

obvious that the fracture distribution affects the pressure distribution as well as saturation profile at different PVI.

A comparison study is performed to show the difference of pore volume production in different fracture distributions. Figures. 19 and 20 display the relations of pore volume injection versus pore volume production and the volume fraction of water. In Figure. 19 ($k_r = 10^5$), the production is relatively high when $\theta = 90°$ due to the vertical fractures properly drive fluid toward the large-scale fractures, as illustrated in Figure. 18 (bottom). In contrast, the situation is different if $k_r = 10^{-5}$. The vertical fractures no longer play the role of conductive channels, therefore the fluid is blocked around the almost impermeable fractures. In this case, the model of $\theta = 45°$ has a relatively high production. Moreover, the cumulative rate of production in the case of high fracture permeability is faster than that of low permeability.

The influence of the length L_f and number N_f of the middle-scale fractures is investigated in this test. Figures. 21 and 22 depict the simulation results. It appears that different fracture distributions show distinct impacts on the production. The case of $\theta = 0°$ has a relatively slow production rate compared to other cases. Figure. 23 illustrates the variation of the rock matrix permeability in different patterns of the middle-scale fractures. It proves that the component k_{xx} is nearly constant in the case $\theta = 90°$. Similarly, k_{yy} is constant when $\theta = 0°$, with the increase of fracture length. The reason is that the vertical and horizontal fractures enhance k_{xx} and k_{yy}, respectively.

We generate a random permeability field to reproduce the heterogeneity in a porous medium, as shown in Figure. 24. A homogeneous medium is simulated as a comparison. To demonstrate the difference of homogeneous and heterogeneous media, we calculate the pressure difference Δp (unit: MPa) between them. Note that the pressure in homogeneous and heterogeneous cases is denoted as p^{ho} and p^{he}, therefore the difference is $\Delta p = |p^{he} - p^{ho}|$. Figure. 24 (bottom) provides the pressure difference induced by heterogeneity and different fracture distributions ($k_r = 10^5$). It appears that the difference concentrates around the large-scale fractures. To measure the deviation of saturation induced by heterogeneity, the difference between the results of homogeneous and heterogeneous cases is calculated. Saturation in homogeneous and heterogeneous cases is denoted as S^{ho} and S^{he}, therefore $\Delta S = |S^{he} - S^{ho}|$. A ratio is defined as $\Delta S/S^{ho}$. Figure. 25 provides the effect of heterogeneity during injection. Saturation is computed by the cells along the diagonal of the domain in these cases. It indicates that the heterogeneity changes the saturation and may influence the production. Obviously, these impacts depend on the fracture distribution and permeability.

6 Conclusion

This work focuses on numerical investigation of two-phase flow in heterogeneous fractured porous media. We combine the discrete fracture model and an equivalent continuum approach to achieve a hierarchical modeling with an adaptive time scheme. This method allows the simulation of multiple length fractures with impermeable or conductive property. Based on these, the effects of heterogeneity, multiple scale fractures and fracture distribution on fluid flow are analyzed.

The main conclusions are summarized as follows:

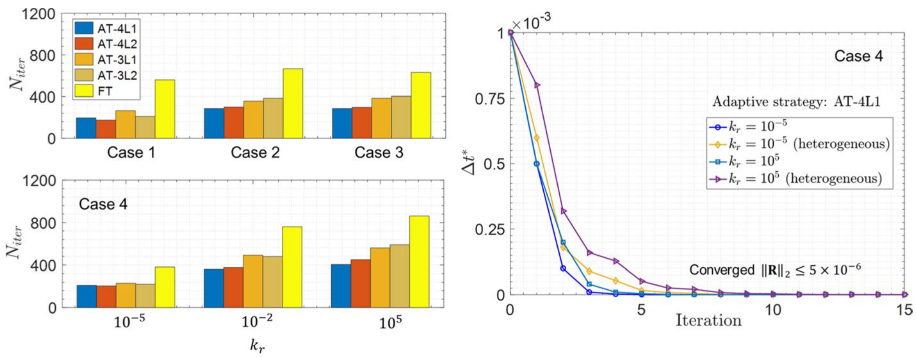

Fig. 15 Comparison of total number of Newton iteration N_{iter} (left) and variation of time step (right) with different adaptive schemes

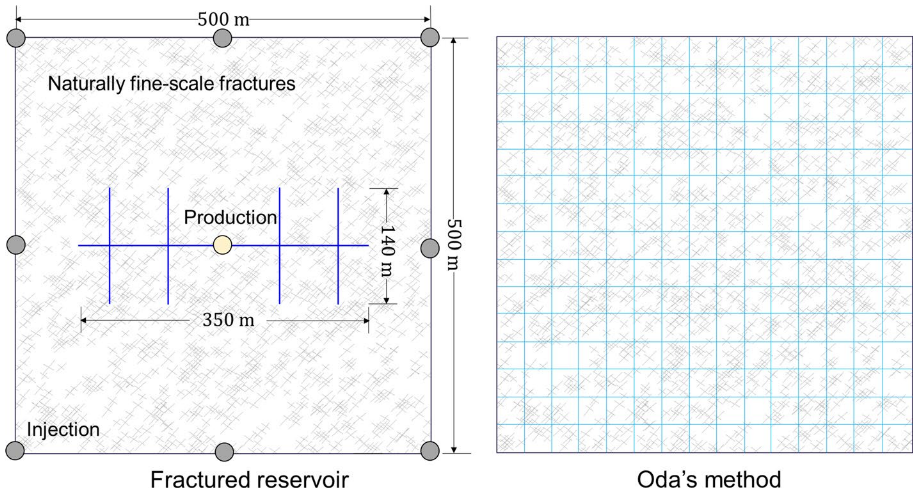

Fig. 16 Schematic of the fractured porous medium and the treatment of fine-scale fractures by Oda's method

Table 3 Statistical parameters of the fine-scale fractures in the reservoir

	Orientation (°)	Length [m]	Number	Distribution
Fracture group 1	40 ~ 55	10 ~ 15	1500	Normal
Fracture group 2	125 ~ 145	5 ~ 10	1500	Normal

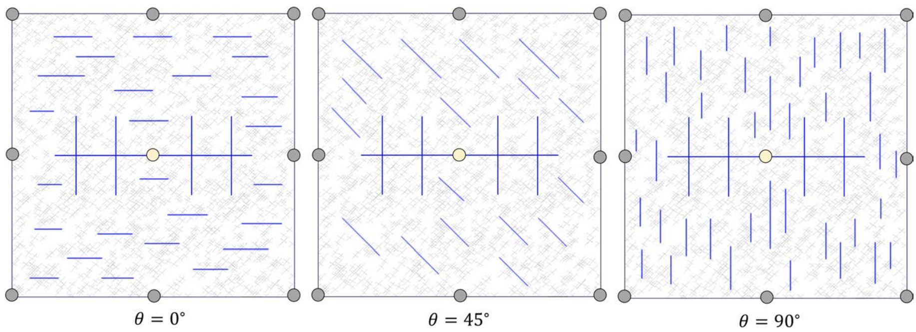

Fig. 17 The fractured porous medium with different angles of the middle-scale fractures

(1) A multilevel adaptive implicit scheme is presented to improve the numerical robustness and efficiency. Different adaptive strategies with 3-levels, 4-levels and fixed time schemes are analyzed to evaluate the computational cost and convergence history. These evaluations prove that our method enjoys several attractive features compared with the classical method.
(2) For a naturally fractured reservoir with many fine-scale fractures, an equivalent continuum approach is integrated in the presented framework to upscale these small fractures, where the equivalent permeability tensor is calculated utilizing the Oda's method.

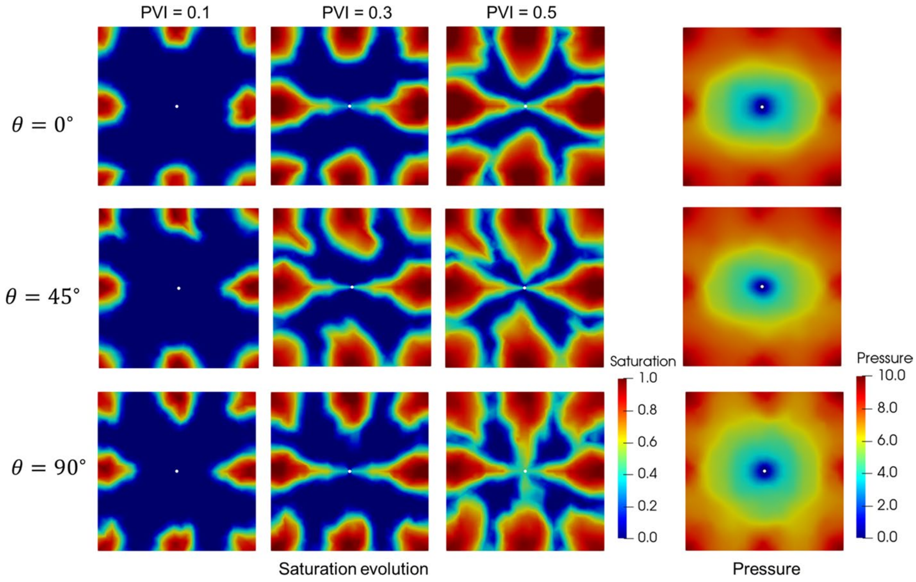

Fig. 18 Saturation evolution and pressure distribution of the fractured porous medium ($k_r = 10^5$)

Besides, the middle-scale fractures are allowed to be set to different angles, while the large-scale fractures are modeled explicitly.

(3) Then, a layer model is constructed with different layer angles. The heterogeneity of permeability field and the initial saturation are considered in the simulation. It appears that the pore volume production is influenced by layer angle and permeability. A porous medium with a fracture network is simulated and the effect of fracture network is analyzed. Next, we study the difference between the fracture network model and the layer model, especially in terms of the pressure distribution and saturation evolution.

(4) Later, a fractured porous medium with multiple length fractures is simulated. The results prove that pore volume production is influenced by fracture distribution and permeability. The impact of the length and number of the middle-scale fractures on permeability of the medium is investigated. The conductivity of the rock matrix is enhanced by the upscaled fine-scale fractures. Pressure difference induced by hetero-

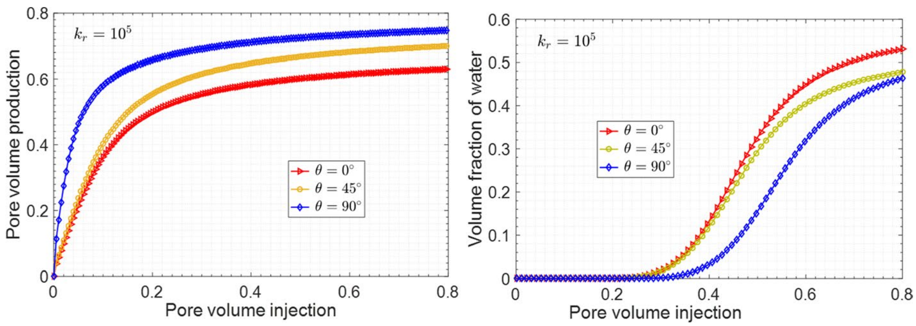

Fig. 19 Curves of pore volume injection (PVI) versus production (left) and PVI versus volume fraction of water (right) when $k_r = 10^5$

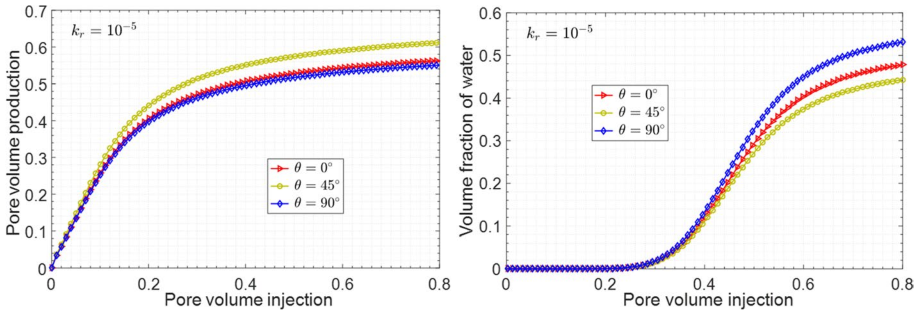

Fig. 20 Curves of pore volume injection (PVI) versus production (left) and PVI versus volume fraction of water (right) when $k_r = 10^{-5}$

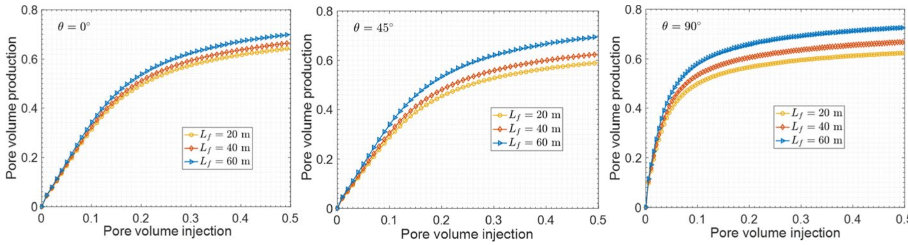

Fig. 21 Effect of length of the middle-scale fractures on production. Curves of pore volume injection (PVI) versus production with different fracture orientations

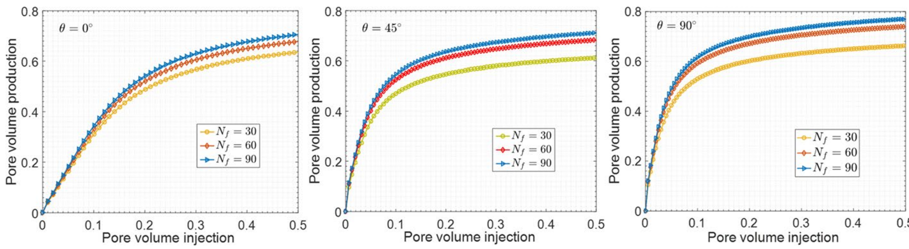

Fig. 22 Effect of number of the middle-scale fractures on production. Curves of pore volume injection (PVI) versus production with different fracture orientations

geneity is analyzed in the situation of different fracture distributions. It appears that the difference is mainly concentrated around the large-scale fractures. The heterogeneity changes the saturation and may influence the production. These impacts depend on the pattern of fracture orientation and permeability.

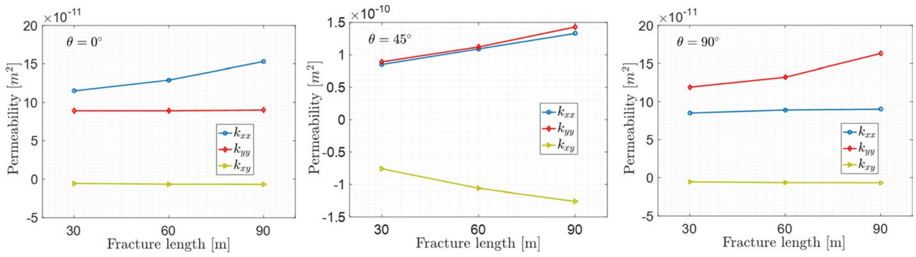

Fig. 23 Variation of permeability in different patterns of the middle-scale fractures

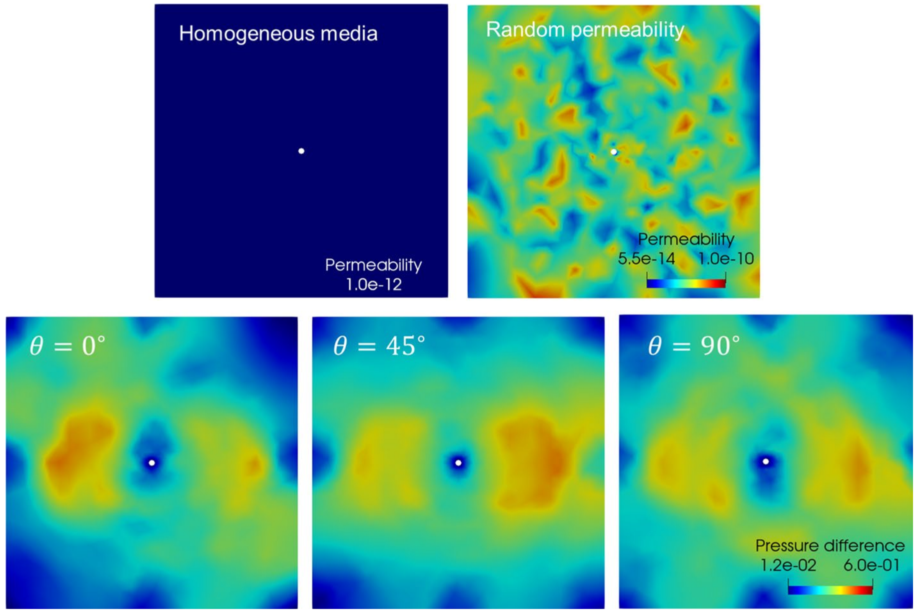

Fig. 24 Different permeability distributions (top) and the pressure difference induced by heterogeneity compared to homogeneous situation (bottom)

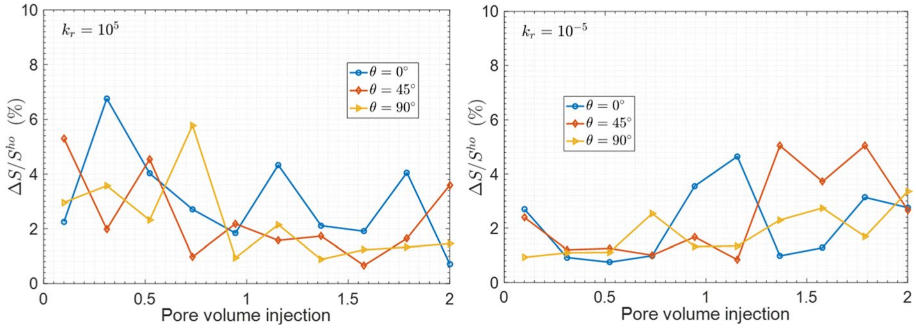

Fig. 25 Saturation deviation induced by heterogeneity compared to homogeneous situation

Appendix A. The Fully Discretized forms of Governing Equations

Following the discussion and notations in Section 3, the fully discretized forms of the governing equations are derived based on Eqs. (7) and (8), which hold true for both fracture and matrix cells in DFM:

(1) The fully discretized form of the elliptic PDE, Eq. (7), is discretized cell-by-cell:

$$\sum_{*=j,k,m,\dots}^{n_i^{neig}} \left[\Lambda_{i*}\left(\eta_i p_i - \eta_* p_*\right)\right]^{n+1} = q_i^{n+1}\Delta V_i \tag{21}$$

where the coefficient Λ_{i*} is defined as $\Lambda_{i*} = \left(\Lambda_{if}\Lambda_{*f}\right)/\left(\Lambda_{if} + \Lambda_{*f}\right)$. Transmissibility Λ_{if} is defined by parameters of two neighboring cells (Karimi-Fard et al. 2004; Berre et al. 2019), for instance, in the case of cell Ω_i^{ele} and its neighbor Ω_*^{ele}:

$$\Lambda_{if} = \frac{\Delta A_{i*}\lambda_t}{D_{i*}\mathbf{n}_{\sigma_*}} \tag{22}$$

where ΔA_{i*} is the area of surface σ_{i*}. D_{i*} is the distance from center of Ω_i^{ele} to center of σ_{i*}. $\mathbf{n}_{\sigma_*}$ is the outward unit vector of edge σ_{i*}. Fig. 3 shows the parameters of fractured cell ω_i^{ele} and its neighbors. It should be noted that the fracture aperture Δa is a virtual value (the dashed lines) which is only considered in the computational aspect instead of the mesh partition.

(2) The fully discretized form of the hyperbolic PDE, Eq. (8), is discretized cell-by-cell:

$$\frac{\phi\Delta V_i\xi_i}{\Delta t}\left(S_i^{n+1} - S_i^n\right) + \underbrace{\sum_{*=j,k,m,\dots}^{n_i^{neig}} \left[f_\uparrow\, \mathbf{u}_{i*}\right]^{n+1}\Delta A_{i*}}_{\text{Upwind term}} = \left[f_i q_i\right]^{n+1}\Delta V_i \tag{23}$$

where ΔV_i is the volume of the cell. Δt is the time step as discussed in Section 4.2. The symbol $f_\uparrow$ in the "Upwind term" represents that it is determined by upwind scheme in Appendix B. Other notations are defined in the preceding sections.

Appendix B. The Upwind Algorithm on Unstructured Grids

It is important to clarify the upwind scheme for calculation of flux, as indicated in Eq. (23). The upwind scheme was originally devised for Cartesian structured grids (LeVeque 1992; Wesseling 2001). In this work, we use it to calculate flux on unstructured grids.

For an arbitrary matrix cell Ω_i^{ele}, the direction of its sub-flux is determined by the velocity at the interface between Ω_i^{ele} and its neighbors Ω_*^{ele} $(*= j, k, m)$, as illustrated in Fig. 3. The upwind algorithm for a matrix cell reads:

$$\left[f_\uparrow \mathbf{u}_{i*}\right]^{n+1} = \begin{cases} \left[f_i \mathbf{u}_{i*}\right]^{n+1} & \text{if flux } \Omega_i^{ele} \rightarrow \Omega_*^{ele} \\ \left[f_* \mathbf{u}_{i*}\right]^{n+1} & \text{if flux } \Omega_*^{ele} \rightarrow \Omega_i^{ele} \end{cases} \tag{24}$$

For an arbitrary fracture cell ω_i^{ele}, the situation is complex. The difficulty is the treatment of different patterns of fracture cells, as shown in Fig. 26. It can be seen from this figure that

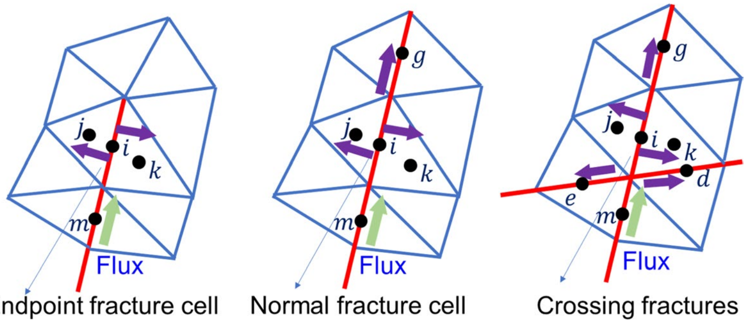

Fig. 26 Different situations of fracture cells when applying the upwind scheme on unstructured grids

different types of ω_i^{ele} would lead to different neighbor patterns. The fluxes toward its corresponding neighbors depend on their pressure gradients. Each crossing fractures cell has six neighbors ω_*^{ele} ($*= j, k, m, e, d, g$), as illustrated in Fig. 26. Eq. (24) is still valid in this case.

The function $f_\uparrow$ is related to saturation (Aziz 1979; Hoteit and Firoozabadi 2008b), as discussed in Section 2. The velocity $\mathbf{u}_{i*}$ is calculated based on Darcy's law:

$$\mathbf{u}_{i*} = \frac{\Lambda_{i*}}{\Delta A_{i*}}\left(\eta_i p_i - \eta_* p_*\right) \tag{25}$$

The value of Λ_{i*} is updated during the iteration process, as discussed in Section 4. Algorithm 2 shows the procedure of the upwind scheme and flux calculation of matrix and fracture cells on unstructured grids.

Algorithm 2 Calculation of flux of matrix and fracture cells on unstructured grids

for each $i \in [1, N_f]$ **do**
  Fracture f_i is determined by its coordinate (x_i, y_i)
  Obtain the grid connectivity $\Omega = \left(\cup_{i=1}^{n^m}\Omega_i^{ele}\right) \cup \left(\cup_{j=1}^{n^f}\omega_j^{ele}\right)$
end for
Define $n^{all} = n^m + n^f$
for each $i \in [1, n^{all}]$ **do**
  if cell $i \in \omega^{ele}$ **then**
    Classify the type of fracture cell ω_i^{ele}: crossing, endpoint or normal cell shown in Fig. B.26
    Calculate velocity at each sub-edge of ω_i^{ele} using Eq. (B.2)
    Calculate flux term $[f_\uparrow \mathbf{u}_{i*}]$ using Eq. (B.1)
  end if
  if cell $i \in \Omega^{ele}$ **then**
    Calculate velocity at the interface between Ω_i^{ele} and its neighbors using Eq. (B.2)
    Calculate flux term $[f_\uparrow \mathbf{u}_{i*}]$ using Eq. (B.1)
  end if
end for

Appendix C. The Discretized forms of Jacobian

Following the discussion in Section 4, the discretized forms of Eq. (13) are expressed as follows based on Eqs. (11) and (12):

$$\left(\Delta V_i q_i^v \frac{\partial f_i}{\partial S_i}\bigg|^v - \frac{\phi \Delta V_i}{\Delta t}\right)\delta S_i^{v+1} - \sum_{*=j,k,m,...}^{n_i^{neig}} \left(\frac{\partial f_\uparrow}{\partial S_\uparrow}\bigg|^v u_{i*}^v \Delta A_{i*}\right)\delta S_\uparrow^{v+1}$$
$$= -\left[f_i q_i\right]^v \Delta V_i + \frac{\phi \Delta V_i}{\Delta t}\xi_i\left(S_i^v - S_i^n\right) + \sum_{*=j,k,m,...}^{n_i^{neig}} \left[f_* u_{i*}\right]^v \Delta A_{i*} \tag{26}$$

for matrix cells, and:

$$\underbrace{\left(\Delta L_i \Delta a_i q_i^v \frac{\partial f_i}{\partial S_i}\bigg|^v - \frac{\phi \Delta L_i \Delta a_i}{\Delta t}\right)}_{\text{Elements of Jacobian}} \mathbf{J}\delta S_i^{v+1} - \underbrace{\sum_{*=j,k,m,...}^{n_i^{neig}} \left(\frac{\partial f_\uparrow}{\partial S_\uparrow}\bigg|^v u_{i*}^v \Delta l_{i*}\right)}_{\text{Elements of Jacobian}} \mathbf{J}\delta S_\uparrow^{v+1}$$
$$= \underbrace{-\left[f_i q_i\right]^v \Delta V_i + \frac{\phi \Delta L_i \Delta a_i}{\Delta t}\xi_i\left(S_i^v - S_i^n\right) + \sum_{*=j,k,m,...}^{n_i^{neig}} \left[f_* u_{i*}\right]^v \Delta l_{i*}}_{\text{Residual,}} - \mathbf{R} \tag{27}$$

for fracture cells. Δl_{i*} is determined by the upwind scheme as discussed in Appendix B. If the velocity is of fracture-fracture, $\Delta l_{i*} = \Delta a_i$; if the velocity is of matrix-fracture, $\Delta l_{i*} = \Delta L_i$. Other notations are defined in the preceding sections.

Acknowledgements This research is financially supported by the Hong Kong Polytechnic University Strategic Importance Fund (ZE2T) and Project of Research Institute of Land and Space (CD78). Financial support of National Natural Science Foundation of China (No. 51991392) is also acknowledged. Lu-Yu Wang thanks Prof. Zhen-Yu Yin at The Hong Kong Polytechnic University for the valuable advice, guidance, corrections of this work, and the fruitful discussion in his team GeoInvention.

Declarations

Conflict of interest The authors declare that they have no known competing financial interests or personal relationships that could have appeared to influence the work reported in this paper.

References

Adler, P..M.., Thovert, J..F., Mourzenko, V..V.: Fractured Porous Media. Oxford University Press, United Kingdom (2013). https://doi.org/10.1093/acprof:oso/9780199666515.001.0001

Ahmed, R., Edwards, M.G., Lamine, S., Huisman, B.A.H., Pal, M.: CVD-MPFA full pressure support, coupled unstructured discrete fracture–matrix Darcy-flux approximations. J. Comput. Phys. **349**, 265–299 (2017). https://doi.org/10.1016/j.jcp.2017.07.041

Alikhani, J., Shoghli, B., Bhowmik, U.K., Massoudieh, A.: An Adaptive Time-Step Backward Differentiation Algorithm to Solve Stiff Ordinary Differential Equations: Application to Solve Activated Sludge Models. Am. J. Comput. Math. **6**, 298–312 (2016). https://doi.org/10.4236/ajcm.2016.64031

Aziz, K.: Petroleum Reservoir Simulation. Applied Science Publishers, New York (1979)

Badar, A., Tirumkudulu, M.S.: Mechanics of saturated colloidal packings: a comparison of two models. Transp. Porous. Media. **135**, 457–486 (2020). https://doi.org/10.1007/s11242-020-01483-0

Berre, I., Doster, F., Keilegavlen, E.: Flow in fractured porous media: a review of conceptual models and discretization approaches. Transp. Porous. Med **30**, 215–236 (2019). https://doi.org/10.1007/s11242-018-1171-6

de Borst, R.: Encyclopedia of Computational Mechanics. Wiley (2018)

Brooks, R., Corey A.: Hydraulic Properties of Porous Media. Hydrol Pap, 3. Fort Collins: Colorado State Univ (1964)

Cacas, M.C., Ledoux, E., de Marsily, G., Tillie, B., Barbreau, A., Durand, E., Feuga, B., Peaudecerf, P.: Modeling fracture flow with a stochastic discrete fracture network: calibration and validation: 1. The flow model. Water. Resour. Res. **26**, 479–489 (1990). https://doi.org/10.1029/WR026i003p00479

Choo, J., Lee, S.: Enriched galerkin finite elements for coupled poromechanics with local mass conservation. Method. Appl. Mech. Eng. **341**, 311–332 (2018). https://doi.org/10.1016/j.cma.2018.06.022

Chung, E.T., Efendiev, Y., Leung, W.T., Vasilyeva, M., Wang, Y.: Non-local multi-continua upscaling for flows in heterogeneous fractured media. J. Comput. Phys. **372**, 22–34 (2018). https://doi.org/10.1016/j.jcp.2018.05.038

Dietrich, P., Helmig, R., Sauter, M., Teutsch, G., Hötzl, H., Köngeter, J.: Flow and Transport in Fractured Porous Media. Springer-Verlag, Berlin Heidelberg (2005). https://doi.org/10.1007/b138453

Eymard, R., Gallouët, T., Herbin, R.: Finite volume methods. Handb. Numer. Anal. 7 Elsevier (2000) https://doi.org/10.1016/S1570-8659(00)07005-8

Ganis, B., Kumar, K., Pencheva, G., Wheeler, M.F., Yotov, I.: A global Jacobian method for mortar discretizations of a fully implicit two-phase flow model. Multi. Model. Simul. **12**(4), 401–1423 (2014). https://doi.org/10.1137/140952922

Ghahfarokhi, P.K.: The structured gridding implications for upscaling model discrete fracture networks (DFN) using corrected Oda's method. J. Pet. Sci. Eng. **153**, 70–80 (2017). https://doi.org/10.1016/j.petrol.2017.03.027

Ghorbani, J., Nazem, M., Carter, J.P.: Numerical modeling of multiphase flow in unsaturated deforming porous media. Comput. Geotech. **71**, 195–206 (2016). https://doi.org/10.1016/j.compgeo.2015.09.011

Gupta, P., Duarte, C.A.: Coupled hydromechanical-fracture simulations of nonplanar three-dimensional hydraulic fracture propagation. Int. J. Numer. Anal. Method. Geomech. **42**, 143–180 (2018). https://doi.org/10.1002/nag.2719

Hajibeygi, H., Karvounis, D., Jenny, P.: A hierarchical fracture model for the iterative multiscale finite volume method. J. Comput. Phys. **230**, 8729–8743 (2011). https://doi.org/10.1016/j.jcp.2011.08.021

Hamzehpour, H., Khazaei, M.: Effective permeability of heterogeneous fractured porous media. Transp. Porou. Media. **113**, 329–344 (2016). https://doi.org/10.1007/s11242-016-0696-9

Hosseini, N., Khoei, A.R.: Modeling fluid flow in fractured porous media with the interfacial conditions between porous medium and fracture. Transp. Porou. Media. **139**, 109–129 (2021). https://doi.org/10.1007/s11242-021-01648-5

Hoteit, H., Firoozabadi, A.: Numerical modeling of two-phase flow in heterogeneous permeable media with different capillarity pressures. Adv. Water. Resour. **31**(1), 56–73 (2008). https://doi.org/10.1016/j.advwatres.2007.06.006

Hoteit, H., Firoozabadi, A.: An efficient numerical model for incompressible two-phase flow in fractured media. Adv. Water. Resour. **31**(6), 891–905 (2008). https://doi.org/10.1016/j.advwatres.2008.02.004

Islam, M.S., Manzocchi, T.: A novel flow-based geometrical upscaling method to represent three-dimensional complex sub-seismic fault zone structures into a dynamic reservoir model. Sci. Rep. **9**(1), 1–14 (2019). https://doi.org/10.1038/s41598-019-41723-y

Jha, B., Juanes, R.: A locally conservative finite element framework for the simulation of coupled flow and reservoir geomechanics. Acta. Geotech. **2**, 139–153 (2007). https://doi.org/10.1007/s11440-007-0033-0

Karimi-Fard, M., Durlofsky, L.J., Aziz, K.: An efficient discrete-fracture model applicable for general-purpose reservoir simulators. SPE. J. **9**, 227–236 (2004). https://doi.org/10.2118/88812-PA

Khoei, A.R., Hosseini, N., Mohammadnejad, T.: Numerical modeling of two-phase fluid flow in deformable fractured porous media using the extended finite element method and an equivalent continuum model. Adv. Water. Resour. **94**, 510–528 (2015). https://doi.org/10.1016/j.advwatres.2016.02.017

Lee, S.H., Lough, M.F., Jensen, C.L.: Hierarchical modeling of flow in naturally fractured formations with multiple length scales. Water. Resour. Res. **37**(3), 443–455 (2001). https://doi.org/10.1029/2000WR900340

LeVeque, R.J.: Numerical Methods for Conservation Laws. Birkhäuser, Basel (1992)

Long, J.C.S., Billaux, D.M.: From field data to fracture network modeling: an example incorporating spatial structure. Water. Resour. Res. **23**, 1201–1216 (1987). https://doi.org/10.1029/WR023i007p01201

Medici, G., Smeraglia, L., Torabi, A., Botter, C.: Review of modeling approaches to groundwater flow in deformed carbonate aquifers. Groundwater. **59**(3), 334–351 (2021). https://doi.org/10.1111/gwat.13069

Molins, S., Trebotich, D., Arora, B., Steefel, C.I., Deng, H.: Multi-scale model of reactive transport in fractured media: diffusion limitations on rates. Transp. Porou. Media. **128**, 701–721 (2019). https://doi.org/10.1007/s11242-019-01266-2

Mustapha, H.: A gabriel-delaunay triangulation of 2D complex fractured media for multiphase flow simulations. Comput. Geosci. **18**, 989–1008 (2014). https://doi.org/10.1007/s10596-014-9440-0

Oda, M.: Permeability tensor for discontinuous rock masses. Geotechnique. **35**(4), 483–495 (1985). https://doi.org/10.1680/geot.1985.35.4.483

Pandare, A.K., Luo, H.: A robust and efficient finite volume method for compressible inviscid and viscous two-phase flows. J. Comput. Phys. **371**, 67–91 (2018). https://doi.org/10.1016/j.jcp.2018.05.018

Sahimi, M.: Flow and Transport in Porous Media and Fractured Rock: From Classical Methods to Modern Approaches, 2nd edn. Wiley, Weinheim, Germany (2011). https://doi.org/10.1002/9783527636693

Salinas, P., Pavlidis, D., Xie, Z., Osman, H., Pain, C.C., Jackson, M.D.: A discontinuous control volume finite element method for multi-phase flow in heterogeneous porous media. J. Comput. Phys. **352**, 602–614 (2018). https://doi.org/10.1016/j.jcp.2017.09.058

Shepherd, D., Miles, J., Heil, M., Mihajlović, M.: An adaptive step implicit midpoint rule for the time integration of newton's linearisations of non-linear problems with applications in micromagnetics. J. Sci. Comput. **80**, 1058–1082 (2019). https://doi.org/10.1007/s10915-019-00965-8

Sheth, S.M., Younis, R.M.: Localized linear systems in sequential implicit simulation of two-phase flow and transport. SPE. J. **22**(05), 1542–1569 (2017). https://doi.org/10.2118/173320-pa

Shewchuk, J.R.: Delaunay refinement algorithms for triangular mesh generation. Comput. Geom. Theory. Appl. **22**, 21–74 (2002). https://doi.org/10.1016/S0925-7721(01)00047-5

Tan, X., Chen, W., Wang, L., Yang, J., Tan, X.: Settlement behaviors investigation for underwater tunnel considering the impacts of fractured medium and water pressure. Mar. Georesour. Geotechnol. **39**(6), 639–648 (2021). https://doi.org/10.1080/1064119X.2020.1737279

Ţene, M., Bosma, S.B.M., Al Kobaisi, M.S., Hajibeygi, H.: Projection-based embedded discrete fracture model (pEDFM). Adv. Water. Resour. **105**, 205–216 (2017). https://doi.org/10.1016/j.advwatres.2017.05.009

Wang, Y., Hajibeygi, H., Tchelepi, H.A.: Algebraic multiscale solver for flow in heterogeneous porous media. J. Comput. Phys. **259**, 284–303 (2014). https://doi.org/10.1016/j.jcp.2013.11.024

Wang, L., Chen, W., Tan, X., Tan, X., Yuan, J., Liu, Q.: Evaluation of mountain slope stability considering the impact of geological interfaces using discrete fractures model. J. Mt. Sci. **16**, 2184–2202 (2019). https://doi.org/10.1007/s11629-019-5527-3

Wang, L., Chen, W., Tan, X., Yang, J.: The impact of various crack geometrical parameters on stress field over tip under different mixed loading conditions and inclination angles. Theor. Appl. Fract. Mech. **102**, 239–254 (2019). https://doi.org/10.1016/j.tafmec.2018.12.001

Wang, L., Chen, W., Tan, X., Tan, X., Yang, J., Yang, D., Zhang, X.: Numerical investigation on the stability of deforming fractured rocks using discrete fracture networks: a case study of underground excavation. Bull. Eng. Geol. Environ. **79**, 133–151 (2020). https://doi.org/10.1007/s10064-019-01536-9

Wang, L., Chen, W., Vuik, C.: Hybrid-dimensional modeling for fluid flow in heterogeneous porous media using dual fracture-pore model with flux interaction of fracture-cavity network. J. Nat. Gas. Sci. Eng. **100**, 104450 (2022). https://doi.org/10.1016/j.jngse.2022.104450

Wang, X.: Finite Element Method. Tsinghua University Publishing Company, Beijing (2003)

Wesseling, P.: Principles of Computational Fluid Dynamics. Springer-Verlag, Berlin Heidelberg (2001)

Liu, Y., Cai, J., Sahimi, M., Qin, C.: A study of the role of microfractures in counter-current spontaneous imbibition by lattice boltzmann simulation. Transp. Porou. Media. **133**, 313–332 (2020). https://doi.org/10.1007/s11242-020-01425-w

Zidane, A., Firoozabadi, A.: Higher-order simulation of two-phase compositional flow in 3D with non-planar fractures. J. Comput. Phys. **402**, 108896 (2020). https://doi.org/10.1016/j.jcp.2019.108896

Zienkiewicz, O., Taylor, R., Zhu, J.Z.: The Finite Element Method: its Basis and Fundamentals, 7th edn. Elsevier (2013). https://doi.org/10.1016/C2009-0-24909-9

Authors and Affiliations

Lu-Yu Wang[1,5] · **Wei-Zhong Chen**[2] · **Yan-Jun Zhang**[4] · **Xiao-Dong Zhang**[5] · **Cornelis Vuik**[3]

Wei-Zhong Chen
zhenyu.yin@polyu.edu.hk

Yan-Jun Zhang
wzchen@whrsm.ac.cn

Xiao-Dong Zhang
15010058869@163.com

Cornelis Vuik
c.vuik@tudelft.nl

1 Department of Civil and Environmental Engineering, The Hong Kong Polytechnic University, Hung Hom, Kowloon, Hong Kong, China

2 Institute of Rock and Soil Mechanics, Chinese Academy of Sciences, 430071 Wuhan, China

3 Department of Applied Mathematics, Delft University of Technology, 2628CD Delft, The Netherlands

4 College of Petroleum Engineering, Xi'an Shiyou University, 710065 Xi'an, China

5 GeoRessources Lab., UMR 7359, CNRS, 54500 Vandoeuvre-lès-Nancy, France